ARTICLE IN PRESS

Geoscience Frontiers xxx (xxxx) xxx

Contents lists available at ScienceDirect

Geoscience Frontiers

journal homepage: www.elsevier.com/locate/gsf

Research Paper

Wave velocities and anisotropy of rocks: Implication for origin of low velocity zone of the Qinling Orogenic Belt, China

Lei Liu [a], Ying Li [a,*], Tingting Li [b], Hanyu Wang [a,c], Shasha Liu [d], Panpan Zhao [a], Gerile Naren [a], Li Yi [a], Hong Liu [a], Fengxia Sun [a], Jianguo Du [a]

[a] United Laboratory of High-Pressure Physics and Earthquake Science, Institute of Earthquake Forecasting, China Earthquake Administration, Beijing 100036, China
[b] Shandong Provincial No. 3 Exploration Institute of Geology and Mineral Resources, Yantai 264004, Shandong, China
[c] School of Earth Sciences and Resources, China University of Geosciences, Beijing 100083, China
[d] Shanghai Supercomputer Center, Shanghai 201203, China

ARTICLE INFO

Article history:
Received 11 April 2024
Revised 6 August 2024
Accepted 25 September 2024
Available online xxxx

Keywords:
Wave velocity of rock
Anisotropy
Origin of low velocity zone
The Qinling Orogenic Belt

ABSTRACT

Structure and composition of Earth is of fundamental importance in exploring the dynamic evolution of the crust and mantle. The Qinling Orogenic Belt (QOB) is located between the North China plate and the South China Plate, and is one of the main orogenic belts in China. To explore the composition and origin of anisotropy and the low wave velocity zone of the QOB, ten rock samples (gneiss and schist) were collected from the five sites of the QOB and the *P*- and *S*-wave velocities of these samples were measured under 0.6 to 2.0 GPa and 100 to 550 °C. The wave velocities increase with increasing pressure and decreasing temperature. The V_P and V_S of the schist and gneiss match the velocity of the middle and lower crust of the QOB, indicating that schist and gneiss are important component of the QOB. All the schist and gneiss samples exhibit obvious seismic anisotropy with 1.64%–17.42% for V_S and 2.93%–14.78% for V_P under conditions of crust and upper mantle. The CPO/LPO and layering distribution of mica in rock samples are the main reasons for this anisotropy. The V_S structures below the five sampled sites from seismic ambient noise tomography were built to explore the effect of schist and gneiss on the composition and structure of the QOB. The results indicate that orientation-arranged gneiss and schist driven by the tectonic stresses might be a new origin of the character of V_P/V_S, seismic anisotropy, and the low velocity zone in the QOB.

1. Introduction

The knowledge of structure, composition and physical property of Earth is of fundamental importance in exploring the movement and dynamic changes of Earth's surface and interior. In-situ measurements of rock velocity under high pressure and high temperature play an important role in understanding the properties of Earth's interior. Generally, seismology data provide a good understanding of the constituent structure and physical state of the Earth's interior. The relationship between geophysical/seismic observations and the composition of the Earth's structure is grounded in two primary factors: (1) measurements of representative natural samples from the crust and mantle, and (2) constraints derived from physical property measurements of minerals and rocks conducted in laboratories. By integrating seismic data structures with petrological interpretations, the resolution of seismic wave velocities and the anisotropic structures of the crust and mantle has been refined through advanced seismic observation techniques. This interpretation largely depends on an understanding of the seismic characteristics of candidate rocks and minerals from Earth's depths, as well as the variations in these properties under internal conditions such as pressure and temperature (Xie et al., 1993; Christensen and Mooney, 1995; Zandt and Ammon, 1995). Many studies have been done on the composition of the mantle and crust by combining seismic wave velocity profiles and laboratory measurements of the elastic wave velocity of various natural minerals (Christensen and Mooney, 1995; Ishikawa and Arima, 2009). By measuring the shear wave velocity (S-wave, V_S) and compressional wave velocity (P-wave, V_P) of rock minerals under various temperatures and pressures, one can interpret geophysical imaging results (Birch, 1961; Almqvist and Mainprice, 2017). For instance, utilizing the velocity data of rocks under high temperatures and pressures in conjunction with seismic velocity

* Corresponding author.
E-mail address: liying@ief.ac.cn (Y. Li).

https://doi.org/10.1016/j.gsf.2024.101939
1674-9871/

Please cite this article as: L. Liu, Y. Li, T. Li et al., Wave velocities and anisotropy of rocks: Implication for origin of low velocity zone of the Qinling Orogenic Belt, China, Geoscience Frontiers, https://doi.org/10.1016/j.gsf.2024.101939

profiles can elucidate the petrological model of the Izu-Bonin-Mariana (IBM) island arc structure (Ishikawa and Arima, 2009). However, such interpretations are not exclusive in some instances, as rocks of varying compositions can exhibit similar wave velocities; furthermore, if a rock is anisotropic, it can exhibit a wide range of wave velocities (Christensen, 1965). Seismic anisotropy is the directional dependence of the velocity of seismic waves in a medium (rock) within the Earth. It has been widely observed in the crust and upper mantle (Fouch and Rondenay, 2006; Long, 2013; Zhao et al., 2016; Lee et al., 2023; Han et al., 2024; Priestley et al., 2024). Zertani et al. (2020) observed that the anisotropy of P-wave velocity on a kilometer scale was 3% to 4%, indicating a back azimuthal dependence of seismological images of the Indian lower crust underthrusting beneath the Himalaya. Nábělek et al. (2009) and Schulte-Pelkum et al. (2005) also observed a back azimuthal dependence of the retrieved signal in the lower crust beneath the Himalaya, which is characterized by a significant large-scale anisotropic fabric within the lower continental crust of India.

The Qinling Orogenic Belt (QOB) is one of the main orogenic belts in China (Matte et al., 1985), located in the central part of the China Central orogenic belt between the North China Block and the South China Block. It trends WNW–ESE in central China and links the Kunlun and Qilian orogens to the west and the Dabie-Sulu Orogen to the east (Zhang et al., 2001; Ratschbacher et al., 2003). The QOB contains two sutures (the Shangdan and Mianlue) and three blocks (Fig. 1). The Shangdan suture separates the North China block (including the North QOB) from the Qinling microplate (the southern QOB), whilst the Mianlue suture separates the Qinling microplate from the South China block. The Shangdan suture is generally considered to be the result of a Middle Paleozoic collision of the North China block and the southern QOB, resulting in a multistage accretion of the southern QOB to the northern QOB (Meng and Zhang, 2000). The Mianlue suture was formed by the early Mesozoic (Triassic) collision between south Qinling and south China block (Zhang et al., 2004). The northern QOB is composed predominately of Proterozoic Kuanping group and Qinling complex, Palaeozoic Erlangping group, and Dengfeng group. The strata is predominantly composed of medium-grade metasedimentary and metavolcanic rocks. The Qinling complex constitutes the Precambrian basement at the northern QOB that underwent strong Proterozoic and Palaeozoic tectonothermal events (You et al., 1993; Wang et al., 2005b). The southern QOB is composed of a thick pile of Late Proterozoic to Triassic sediments. Palaeozoic and Mesozoic intrusions occur widely in the northern QOB. The Palaeozoic intrusions are regarded as the products of subduction and collision between the northern and southern QOB, while the Mesozoic intrusions are related to Early Mesozoic collision between the North and South China blocks (Xue et al., 1996; Wang et al., 2009).

The seismic reflection/refraction, surface wave tomography, and receiver function studies have been used to investigate the crustal and upper mantle structures of the Qinling Orogenic Belt (QOB) and surrounding areas by Li et al. (2015), Yuan (1996), and Song et al. (2018). The ductile flow, strike-slip faults with displacement from tens to hundreds of kilometers, and widespread extension indicate that the QOB has undergone significant reactivation since the Cretaceous period (Zhang et al., 1989; Ratschbacher et al., 2003; Enkelmann et al., 2006). Song et al. (2017) used high-resolution three-dimensional observations to reveal that the Qinling Orogenic Belt (QOB) has a special flyover crustal structure with an E–W trending high-velocity structure in the upper crust (0–10 km), a transitional zone in the middle crust (10–30 km), and an approximately N–S trending low-velocity zone in the middle-lower crust (20–40 km). Teng et al. (2014) found the upper crust P-wave velocity of QOB exhibits significant lateral heterogeneity, which extends down to the top of the lower crust and upper mantle or deeper; and the vertically and horizontally wave velocity changes are inhomogeneous and non-linear in the lower crust and upper mantle. Liu et al. (2006) observed low V_P and Poisson's ratio from a seismic deep refraction profile beneath the western QOB. Lei and Zhao (2016) revealing a low-velocity anomalies in the upper mantle and some low-velocity anomalies in the uppermost mantle with a fast-wave direction parallel to the QOB by Pn

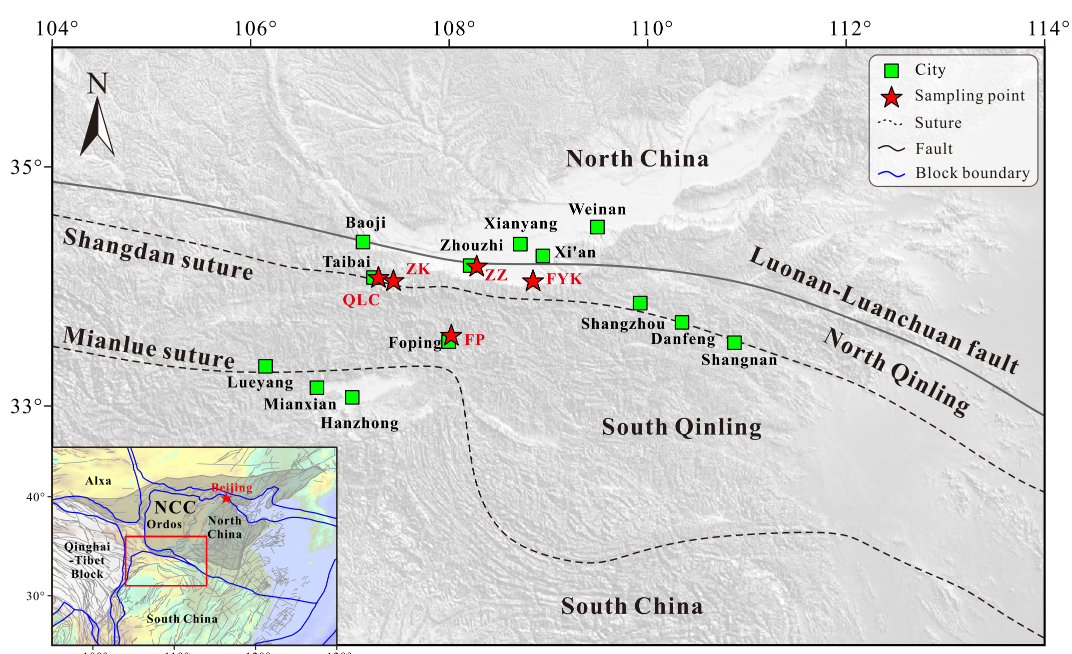

Fig. 1. The schematic geologic tectonics of the QOB and the sampled sites. Insert showing the tectonic blocks and the location of studying area; NCC is North China Craton; the stars are the sample sites following as Qilichuan, Taibai County, Baoji City (QLC); Zuikou, Taibai County, Baoji City (ZK); Zhouzhi County, Xi'an City (ZZ); Fengyukou, Xi'an City (FYK); Foping County, Hanzhong City (FP), Shanxi Province.

tomography (Zhou and Lei, 2016). Wei et al. (2020) observed local low-velocity anomalies in the middle-lower crust in the western Qinling Orogenic Belt (QOB) and the Qilian orogen. They also observed high S-wave velocities in the middle-lower crust at the juncture region between the western QOB and the Qinling-Dabie orogen. Seismic studies revealed a low-velocity anomaly extending from 100 to 320 km below the QOB (Bao et al., 2015; Wei et al., 2016; Zhang et al., 2018). The data of experimentally measured V_P of rocks (plagioamphibolite, volcanic rock, hornblende granulite, marble, mica plagioclase schist) from the QOB indicate that dehydration of minerals and partial melting of rock may be the reasons for the low velocity layer in the middle and lower crust of QOB (Zhao et al., 1996).

Here, to further explore the composition and origin of anisotropy and the low velocity of the QOB, ten rock samples (gneiss and schist) were collected from the QOB at five different sites and the V_S and V_P of these samples were measured under 0.6–2.0 GPa and 100–550℃. The results indicate that orientation-arranged gneiss and schist caused by tectonic stresses might be the important origin of the seismic anisotropy and the low velocity zone in the QOB.

2. Material and methods

2.1. Rock samples

Ten rock samples (gneiss and schist) were collected from the QOB at five different sites, Fengyukou, Qilichuan, Zuikou, Foping and Zhouzhi (Fig. 1). Two rock samples were gathered at each sampling site. Table 1 provides the locality, lithology and results of chemical analyzes and X-ray diffraction (XRD) and X-ray Fluorescence Spectrometer (XRF) of each rock sample studied. The typical modal compositions are mainly quartz, albite, microcline, mica (biotite, muscovite), chlorite, amphibole, and magnetite. Other mineral compositions less than 1% are not listed. The results of chemical analyze show that the compositions are mainly SiO_2, Al_2O_3, Fe_2O_3, K_2O, CaO, Na_2O, TiO_2, MgO. Other chemical compositions less than 0.1% are not listed.

2.2. Experimental methods

The wave velocities of the rock samples were measured using the YJ-3000 Press, which is located in the key laboratory of the high-temperature and high-pressure study of the Earth' s interior, the Institute of Geochemistry, Chinese Academy of Sciences. The rock samples were prepared into the cylinder specimens with a diameter of 10 mm in diameter and a length of 6 mm (Fig. 2). The wave velocities were determined by the pulse transmission/reflection method (Xie et al., 1993; Liu et al., 2000). The pressure of the apparatus is calibrated with the melting curve of copper determined by the differential thermal analysis method and from the quartz–coesite transition. The pressure is considered accurate to 1.5% (Xie et al., 1993). The temperature is calibrated with a NiCr–NiSi thermocouple. The uncertainty in temperature measurement is less than ±5°C (Zhou et al., 2011). The length of sample are determined as follows: (1) When pressurized, the sample length (L) is corrected under high pressure, $L/L_0 = 1 - [P/(3\ K_0)]$, where L_0 is original length of 6 mm and K_0 is adiabatic bulk modulus of rock (51 GPa); (2) At constant pressure heating, the travel time (T) is measured, and it is assumed that the wave velocity when the sample is heated and then cooled to room temperature is equal to the wave velocity (V) at room temperature at constant pressure, so that the length of the sample after constant pressure heating is known as $L = V \times T$. The maximum error of this method here used for measuring the wave velocity is less than 1.2% (Liu et al., 2002).

To investigate the differences in wave velocity of rocks in various tectonic directions, three experimental samples were prepared for each rock sample: parallel to its foliation (x), perpendicular to its foliation (y), and at a 45° angle to its foliation (z) (Fig. 2). In this study, foliation is defined by the strong shape preferred orientation (SPO) of the platy and elongated mica minerals. Under high-pressure and high-temperature, the V_P and V_S were measured for

Table 1
Chemical and mineral composition of the rock samples.

Chemical composition (wt.%)

Sample	SiO_2	Al_2O_3	Fe_2O_3*	K_2O	CaO	Na_2O	TiO_2	MgO	Total
ZK01	62.43	13.64	11.54	4.11	2.54	1.11	0.95	0.75	97.07
ZK02	65.14	13.11	12.27	3.34	2.12	1.43	0.81	0.49	98.71
ZZ01	68.14	12.67	6.12	5.61	2.31	1.24	0.62	1.15	97.86
ZZ02	64.39	12.34	5.61	6.14	3.11	1.68	0.84	1.68	95.79
FYK01	64.41	11.42	10.28	6.99	2.43	2.21	0.249	1.15	99.13
FYK02	62.87	12.57	10.98	6.12	2.78	2.01	0.21	1.13	98.67
QLC01	63.56	12.2	11.72	4.55	2.39	1.23	0.973	0.651	97.27
QLC02	60.46	12.33	13.97	4.73	2.22	1.44	1.08	0.835	97.07
FP01	60.51	16.37	6.78	4.12	2.14	8.11	0.66	0.84	99.53
FP02	64.14	14.51	4.67	3.14	3.11	7.41	0.51	0.61	98.10

Modal composition (wt.%)

Sample	Qz	Ab	Mc	Mica	Chl	Am	Mag	Location (Shanxi province)	Lithology
ZK01	64	18	5	8	4			Qilichuan, Taibai County,	schist
ZK02	65	19	3	9	3			Baoji City	
ZZ01	48	27	10	12		3		Zuikou, Taibai County,	
ZZ02	43	25	12	15		5		Baoji City	
FYK01	46	30	10	11	3			Zhouzhi County	
FYK02	44	32	8	13	3			Xi'an City	
QLC01	49	31	7	10	3			Fengyukou	gneiss
QLC02	47	32	9	9	3			Xi'an City	
FP01	33	31	8	16		6	5	Foping County	
FP02	31	32	10	17		4	4	Hanzhong City	

Notes: * Means the total Fe including FeO + Fe_2O_3. Abbreviations of mineral list in the table as follows: Quartz, Qz; Albite, Ab; Microcline, Mc; Chlorite, Chl; Amphibole, Am; Magnetite, Mag.

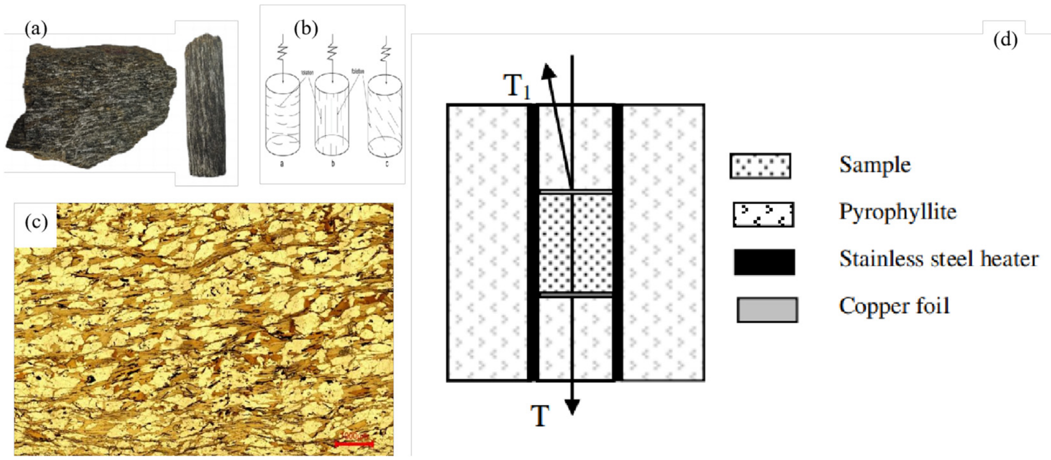

Fig. 2. The diagrams of the selected rock samples, microphotographs and sample assembly. (a) Selected primitive rock sample and experiment sample; (b) Schematic experiment samples from 3 different direction, a, b, and c indicate that samples made from parallel to its foliation (x), perpendicular to its foliation (y), and is at a 45° angle to its foliation (z) and the measured results labeled as Vx, Vy, and Vz, respectively; (c) The microphotograph of foliation structure; (d) The sample assemble.

the rock samples in three different directions (x, y, and z). At room temperature, the pressure applied to the sample was gradually increased from 0.6 GPa to 2 GPa, with measurements taken every 0.2 GPa during this period. Subsequently, the sample was heated to 550 °C and allowed to cool naturally, with measurements taken every 50 °C of cooling.

3. Results and discussion

3.1. The wave velocity under high pressure and temperature

The V_P and V_S of ten samples were measured at pressures ranging from 0.6 GPa to 2.0 GPa and temperatures ranging from 100 °C to 550 °C. Three groups of V_P and V_S were measured for each sample from three directions, and labeled as V_Px, V_Py, V_Pz and V_Sx, V_Sy, V_Sz, respectively.

Fig. 3 illustrates the variations of V_P and V_S of ten samples under different pressures. The V_P and V_S of all samples show an almost linear increase with pressure. For two samples from Foping County, the V_P ranges from 5.74 to 6.39 km/s and 5.83 to 6.51 km/s, while the V_S ranges from 3.31 to 3.89 km/s and 3.35 to 4.00 km/s. For two samples from Fengyukou Ravine, the V_P ranges from 5.63 to 6.16 km/s and 5.72 to 6.31 km/s, while the V_S ranges from 3.11 to 3.42 km/s and 3.12 to 3.41 km/s. For two samples from Qilichuan County, the V_P ranges from 5.45 to 6.40 km/s and 5.48 to 6.46 km/s, while the V_S ranges from 2.98 to 3.61 km/s and 2.99 to 3.63 km/s. For two samples from Zhouzhi County, the V_P ranges from 5.98 to 6.53 km/s and 5.94 to 6.48 km/s, while the V_S ranges from 3.51 to 3.90 km/s and 3.49 to 3.98 km/s. For two samples from Zuikou County, the V_P ranges from 5.49 to 6.53 km/s and 5.51 to 6.57 km/s, while the V_S ranges from 3.28 to 3.98 km/s and 3.31 to 4.01 km/s, all at pressures ranging from 0.6 to 2 GPa.

Fig. 4 presents the variations of V_P and V_S of ten samples with the increasing temperature from 100 °C to 550 °C. The V_P and V_S of all samples exhibit a linear decrease with increasing temperature. For two samples from Foping County, the V_P ranges from 5.99 to 6.39 km/s and 6.00 to 6.41 km/s, while the V_S ranges from 3.29 to 3.88 km/s and 3.26 to 3.90 km/s. For two samples from Fengyukou Ravine, the V_P ranges from 5.87 to 6.15 km/s and 5.90 to 6.22 km/s, while the V_S ranges from 3.22 to 3.37 km/s and 3.16 to 3.44 km/s. For two samples from Qilichuan County, the V_P ranges from 5.80 to 6.40 km/s and 5.82 to 6.44 km/s, while the V_S ranges from 3.22 to 3.61 km/s and 3.23 to 3.60 km/s. For two samples from Zhouzhi County, the V_P ranges from 6.20 to 6.46 km/s and 6.22 to 6.45 km/s, while the V_S ranges from 3.49 to 3.95 km/s and 3.45 to 3.96 km/s. For two samples from Zuikou County, the V_P ranges from 5.55 to 6.51 km/s and 5.58 to 6.54 km/s, while the V_S ranges from 3.21 to 3.85 km/s and 3.23 to 3.88 km/s, all at temperatures ranging from 100 °C to 500 °C.

Two samples collected from one site exhibit similar wave velocity values. However, our measured values of V_P and V_S from three different directions of different samples vary widely; and even for the same sample, the measured V_P and V_S also show different values in different directions. Therefore, to understand differences between different samples, we calculated the average values of V_P ((V_Px + V_Py + V_Pz)/3) and V_S ((V_Sx + V_Sy + V_Sz)/3) at the same pressure or temperature and presented them in Fig. 5. The average wave velocities increase with increasing pressure and decreasing temperature. Under the pressure and temperature explored in this work, the wave velocities of FYK samples that originated in the Fengyukou Ravine are the lowest (except for the V_P of the FYK02), while those of ZZ samples that originated in the Zhouzhi County are the highest. For the other 3 samples, their wave velocities generally follow FP > ZK > QLC.

Three granitic gneiss collected from the Tuofeng, the Dabie-Sulu orogenic belt exhibit V_P values ranging from 6.02–6.08, 6.21–6.25 and 6.24–6.28 km/s under 0.6–0.8 GPa, respectively, with average values of 6.16–6.20 km/s (Wang et al., 2005a). The V_P of gneiss samples collected from Foping (FP) and Fengyukou (FYK) are 5.96–6.00, 6.05–6.09 and 5.73–5.77, 5.81–5.86 km/s under 0.6–0.8 GPa, respectively, with an average V_P of 5.89 –5.93 km/s. Our measured V_P of the gneiss under 0.6–0.8 GPa is slightly smaller than that of the Tuofeng, the Dabie-Sulu orogenic belt (Wang et al., 2005a).

Our measured V_P of gneiss from the Fengyukou Ravine, Zhouzhi County and Zuikou County are in the range of 5.55–6.54 km/s, which are higher than previous results of felsic gneiss from the Yudongzi group with 5.61–5.93 km/s (Zhao et al., 1996) (Fig. 6). The V_P of schist from the Foping County and Qilichuan County are in the range of 5.80–6.44 km/s, which are slightly smaller than previous results of schist from the Yaolinghe group with 5.69–6.65 km/s (Zhao et al., 1996). Our measured V_P of schist from the Foping County is in the range of 5.99–6.41 km/s, which is larger than values of hornblende granulite the Foping group with 5.70–6.62 km/s (Zhao et al., 1996). So, V_P of gneiss and schist measured in this study are close to volcanic rocks, but smaller than values of marble, gabbro and metasediment rocks from the Qinling area (Zhao et al., 1996).

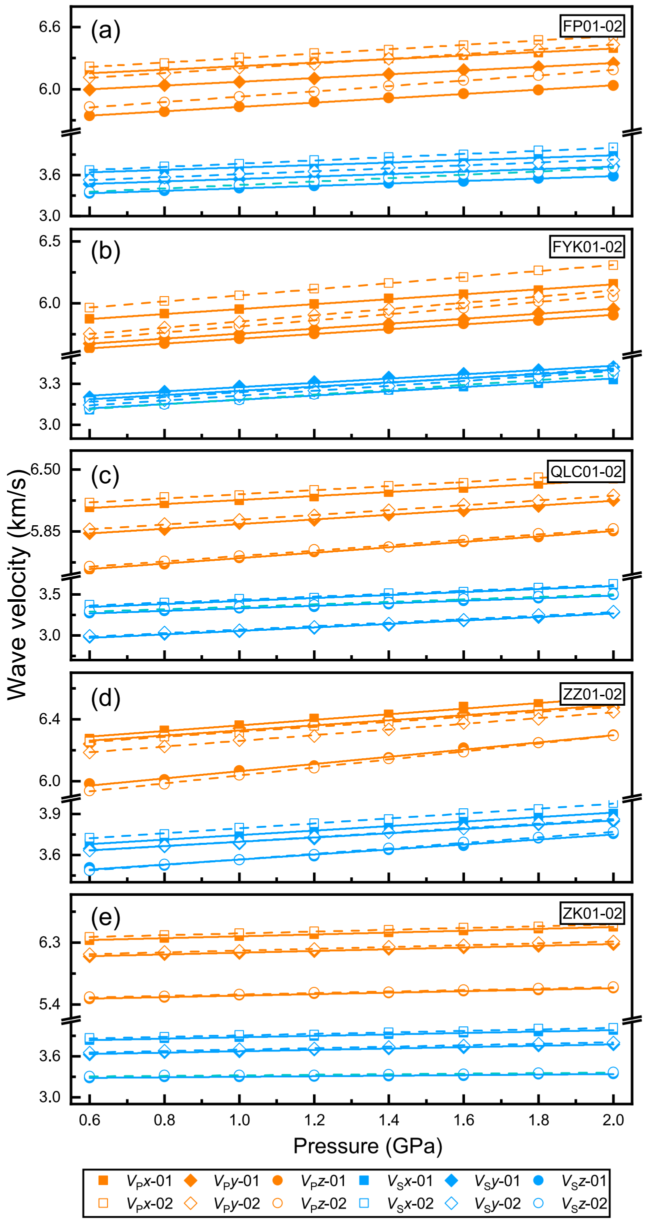

Fig. 3. The wave velocity of rocks under high pressure. (a–e) The velocities of rocks from Foping, Fengyukou, Qilichuan, Zhouzhi and Zuikou, respectively. The results of wave velocity under high pressure are measured at room temperature.

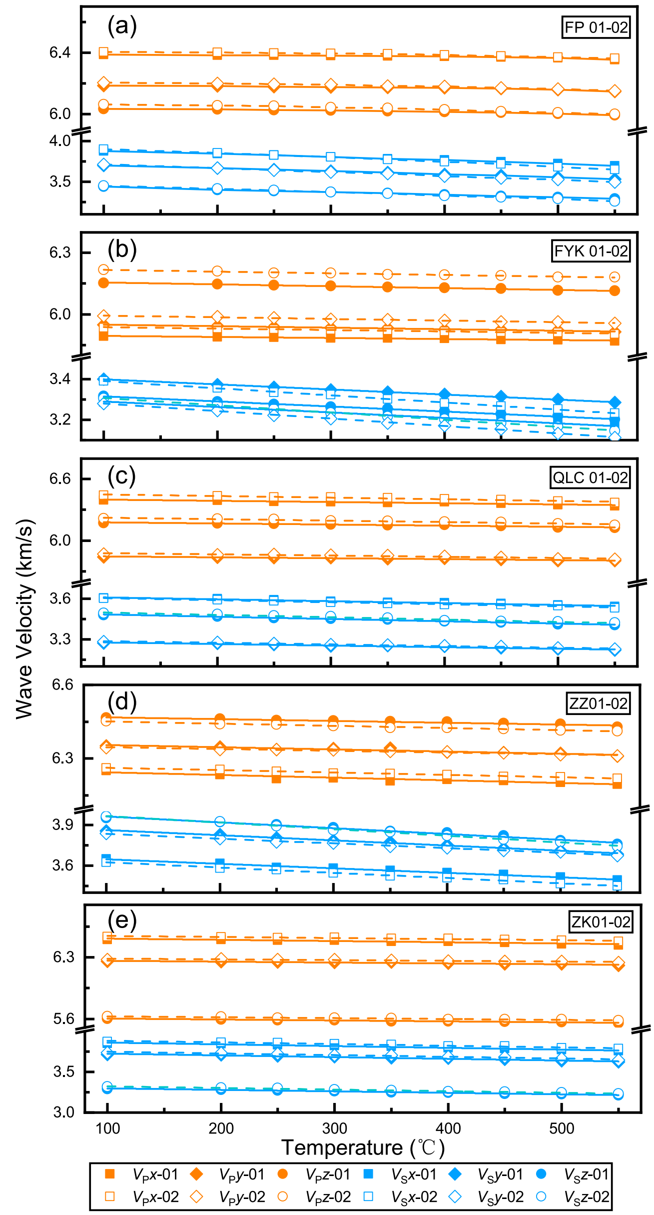

Fig. 4. The wave velocity of rocks under high temperature. (a–e) The velocities of rocks from Foping, Fengyukou, Qilichuan, Zhouzhi and Zuikou, respectively. The wave velocities under high temperature are measured at 2 GPa.

3.2. V_P/V_S ratio

The V_P/V_S ratio of the rock samples were measured and calculated under high pressure and temperature, as shown in Fig. 7. The V_P/V_S ratio decreases with increasing pressure and decreasing temperature.

The values of V_P/V_S decrease by 0.01–0.06 from 0.6 GPa to 2.0 GPa, and increase by 0.01–0.09 from 100 °C to 550 °C. Among all samples, the FYK schist and QLC gneiss have the highest V_P/V_S ratios, which are larger than 1.75; whereas the ZK schist has the lowest V_P/V_S ratio of 1.66. An increase in plagioclase or a decrease in quartz content typically affects the V_P/V_S ratio of rocks (Table 1) (Tarkov and Vavakin, 1982).

The QOB is characterized by a low crustal velocity of 3.6 km/s and a low V_P/V_S ratio of 1.66–1.8, indicating that middle to lower crust is predominantly felsic (Guo and Chen, 2016). Seismic refraction has revealed low V_P and V_P/V_S beneath the western QOB (Liu et al., 2001). The lower crust of the QOB predominantly exhibits intermediate to low V_P/V_S values (<1.8), which indicate that its lower crust should be intermediate to felsic, and also exhibits small volumes of high V_P/V_S (>1.85), which indicate the composition of mafic or bearing fluid (partial melting or water (Ye et al., 2017)). Our measured V_P/V_S indicate that rock samples gathered from the QOB are felsic and mafic (Owens and Zandt, 1997), which is consistent with the analytic result of X-ray diffraction (Table 1) and the result of Guo and Chen (2016) and Liu et al (2001).

Joint inversion of surface wave dispersion and receiver function of a dense linear broadband seismic array shows that the V_P/V_S values of the lower crust vary from 1.78 south of the western QOB to 1.65 north of the western QOB (Li et al., 2022). Our results indicate that schist and gneiss of the QOB may be the origin for the observed character of the V_P/V_S.

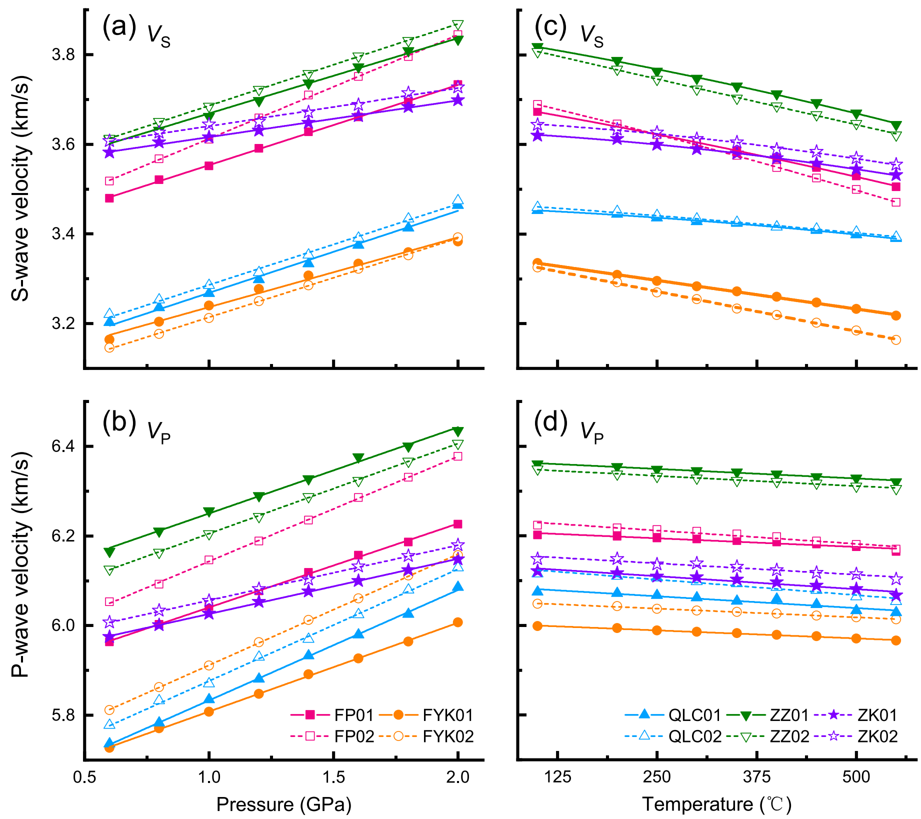

Fig. 5. The wave velocity of rocks under high pressure and high temperature. (a and b) The *Vs* and *Vp* of rocks under high pressure; and (c and d) The *Vs* and *Vp* of rocks under high temperature. The results of wave velocity under high pressure are measured at room temperature and the wave velocities under high temperature are measured at 2 GPa.

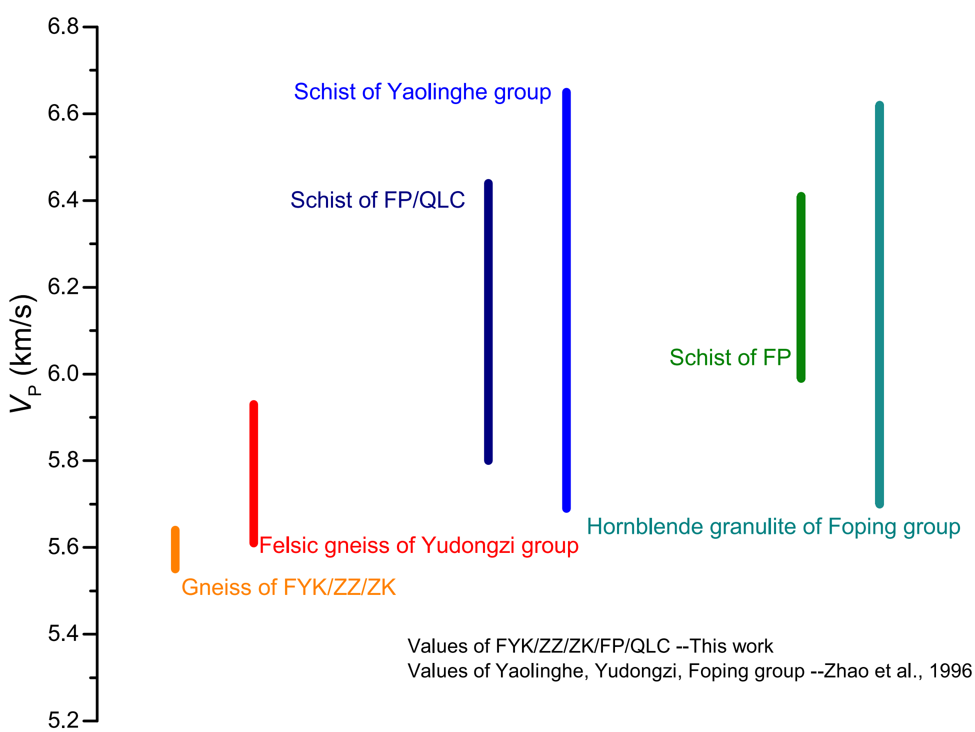

Fig. 6. Comparison of our measured velocities with previous results.

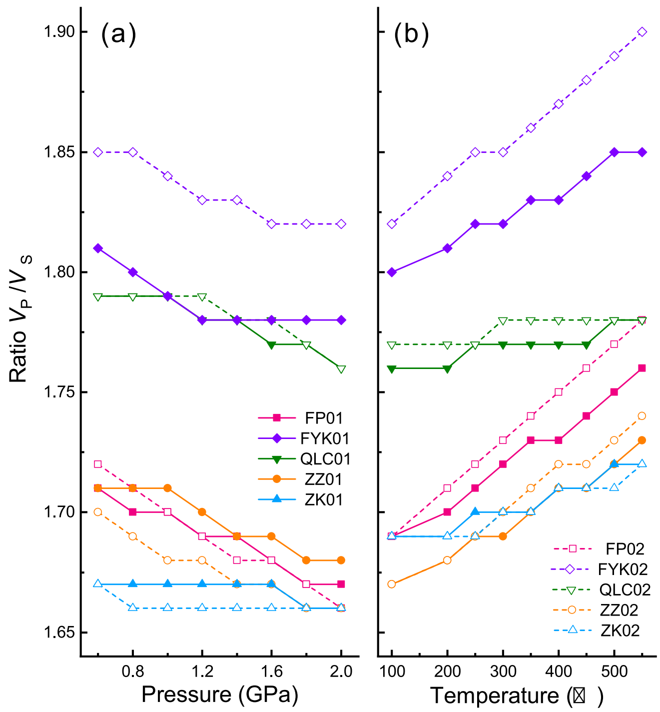

Fig. 7. The V_P/V_S of the rocks under high pressure and high temperature and presented. (a and b) The V_P/V_S of rocks under high pressure and under high temperature, respectively. The results of wave velocity under high pressure are measured at room temperature and the wave velocities under high temperature are measured at 2 GPa.

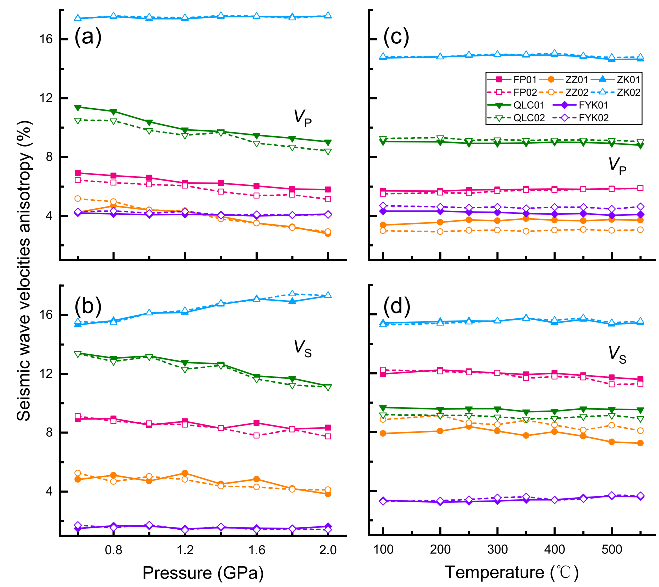

Fig. 8. The anisotropy of wave velocities in rocks under high pressure and temperature. (a and b) The anisotropy of wave velocities in rocks under high pressure and (c and d) under high temperature. The results of wave velocity under high pressure are measured at room temperature and the wave velocities under high temperature are measured at 2 GPa.

3.3. Anisotropy under high pressure and temperature

Seismic anisotropy is often thought of as a proxy to explore the structure and stress states associated with tectonic processes (Silver, 1996). In this study, the anisotropy of rock wave velocity was examined by measuring the V_P and V_S of a rock sample from three different directions (x, y, and z) at high pressure and high temperature; marked as V_Px, V_Py, V_Pz and V_Sx, V_Sy, V_Sz and the details list above. The wave velocities of rock samples from different directions are presented in Figs. 3 and 4, and the wave velocities of a sample generally show the characters of $V_Px > V_Py > V_Pz$ and $V_Sx > V_Sy > V_Sz$ (Figs. 3 and 4), indicating that wave velocities are highest parallel to its foliation (Vx) and lowest perpendicular to foliation (Vz). All rocks measured in this work show obvious seismic anisotropy.

The anisotropy of wave velocity is calculated as a percentage of the ratio of the difference between the maximum and minimum velocities and the average velocity:

$$A = (V_{max} - V_{min})/V_{mean} \times 100\% \quad (1)$$

where V_{mean} is the arithmetic mean of the wave velocities measured from the three directions (x- parallel to foliation, y-perpendicular and z-oblique); and anisotropy of V_P and V_S is marked as AV_P and AV_S, respectively.

The seismic anisotropy of V_P and V_S (AV_P and AV_S) is calculated by the Eq. (1) and presented in Fig. 8. Temperature has a slightly effect on seismic anisotropy. Bazargan et al. (2021) reported a slight increase of 4% in AV_P with increasing temperature from room temperature to 600 °C, which is consistent with our results. The AV_P and AV_S of the QLC and the ZZ, and AV_P of the FP decrease with increasing pressure, while the AV_P and AV_S of the ZK increase with increasing pressure. The AV_P and AV_S of the FYK, and AV_S of the FP remained nearly unchanged with pressure. Seismic anisotropy changed from high to low from Qilichuan and Zuikou of Taibai County, Foping County, Zhouzhi County to Fengyukou of Xi'an City, from west to east of QOB.

Under 100–550 °C and 0.6–2.0 GPa, the ZK schist exhibited the highest anisotropy with AV_P values ranging from 14.65% to 15.07% and 14.23% to 14.78%, and AV_S values ranging from 15.29%–15.76% and 15.33%–17.42%, respectively. The FYK gneiss shows the lowest AV_S values with a range of 3.24% to 3.71% under 100–550 °C and 1.64%–2.69% under 0.6–2.0 GPa. For the AV_P, the ZZ exhibited the lowest values with a range of 3.17%–3.41% under 100–550 °C, while both the ZZ schist and FYK gneiss showed similar AV_P values with a range of 2.93% to 5.14%, which were smaller than the other three rock samples under 0.6–2.0 GPa.

The ten rock samples, including 6 schist and 4 gneiss, were collected which exhibit an obvious foliation structure. The X-ray diffraction (XRD) analysis of the samples revealed that mica is one of the main components of these rock samples (Table 1), and mica is oriented in the rock sample and forms a foliation structure. Previous studies have indicated that mica significantly influences the seismic wave velocity anisotropy of crustal rocks, with the anisotropy primarily determined by the preferred orientation of the mica lattice/crystal (Kitamura, 2006). In foliated gneisses, V_P is highest within the foliation plane. The maximum V_P values is parallel to lineation, and minimum velocity is almost always perpendicular to foliation (Ji and Salisbury, 1993; Kern et al., 2008). This is consistent with our measured character of the seismic anisotropy.

The seismic anisotropy of rock is mainly controlled by (1) the preferred orientation of microcracks, SPO, LPO, CPO, and thin mineral layers with different properties (Kern et al., 2001). Generally, microcrack in rocks would close when the pressure is greater than 0.3 GPa (Hyndman and Drury, 1976; Miller and Christensen, 1997). Since the pressure range in this work is 0.6–2.0 GPa, the effect of microcrack on the seismic anisotropy of rocks can be ignored. Therefore, CPO/LPO and layering distribution of mica in rocks are the main reasons for the anisotropy of V_P and V_S under high pressure and temperature in this work.

Seismic anisotropy is prominent in the QOB. The P-wave velocity of the upper crust in the QOB exhibits obvious lateral heterogeneity (Teng et al., 2014). Gao et al. (2019) split the shear wave and found a two-layer anisotropic structure below the western QOB, and the fast wave velocity of the upper mantle of this region is WNW–ESE. Zhou and Lei (2016) observed some low-velocity anomalies in the uppermost mantle with a fast-wave direction parallel to the QOB by Pn tomography. Radial anisotropy (the wave velocity differences between the vertical and lateral directions) of the P-wave tomography results in the lower crust and uppermost mantle beneath the western QOB show strong anisotropy with 1.5% at a depth of 40 km and 170 km (Li et al., 2022). Huang et al. (2008) reported strong anisotropy with an E–W fast-wave direction in the southern QOB and a shear-wave splitting time delay as large as 1.8 s in the QOB. These seismic anisotropies have been believed to be caused by upper mantle flow or asthenospheric flow (Huang et al., 2008; Gao et al., 2019; Li et al., 2022).

When rocks are deformed in the dislocation regime, mineral grains develop an LPO by dislocation creep, dynamic recrystallization and grain-boundary migration, resulting in seismic anisotropy on a macroscopic scale, for example, the fast velocity of olivine align with the maximum shear direction are generally though as the origin of the seismic anisotropy at the upper mantle, namely, the tectonic stress field plays a critical role in producing crust anisotropy (Zhang and Karato, 1995; Long and Becker, 2010). In this study, it was observed that schist and gneiss exhibit significant seismic anisotropy with 1.64%–17.42% for V_S and 2.93%–14.78% for V_P under conditions of crust and upper mantle. The QOB has experienced significant tectonic activity since the Cretaceous period, including ductile flow, strike-slip faults, and widespread extension and shear movement (Matte et al., 1985; Zhang et al., 1989; Liu et al., 1997; Ratschbacher et al., 2003; Enkelmann et al., 2006). High-pressure-high-temperature experiment shown that V_P and V_S anisotropy arise mainly because of crystallographic preferred orientation with the slowest velocity direction tending to be normal to the foliation (Khazanehdari et al., 2000). A three-dimensional model of crustal and upper mantle anisotropy based on new observations of ambient noise and earthquake data shown that the average anisotropy in the western United States is ~1.3% and the fast directions of shear wave parallel to the San Andreas fault in the uppermost mantle is consistent with the deformation direction induced by simple shear (Lin et al., 2011). Therefore, it is proposed that orientation-arranged schist and gneiss caused by tectonic stresses may be one of reasons for the seismic anisotropy of the QOB.

3.4. Composition of the QOB

Previous works found that the lithosphere of the QOB is significantly heterogeneous with obvious vertical and horizontal changes, and the overall composition of the lithosphere is thought to be granodiorite to quartz diorite and similar to the world average continental crust (Zhang et al., 1997). Zhang et al. (1997) proposed that the lower crust of the QOB is mainly composed of amphibolite – granulite facies gneiss with V_P = 6.49–6.81 km/s, the middle crust is mainly amphibolite – greenschist facies with V_P = 5.71–6.10 km/s and the upper crust is mainly composed of surface rocks with V_P = 5.40–6.08 km/s. The results of seismic tomography show that the QOB crust is divided into three layers, with V_P of the upper crust ranges from 5.02 to 6.15 km/s, values of the middle crust varying between 5.92 and 6.50 km/s, and values of the lower crust change from 6.48 to 6.93 km/s (Yuan, 1996). Our measured V_P of 6 schists (ZZ01-02, ZK01-02 and FYK01-02) are in the range of 5.49–6.57 km/s and those of 4 gneiss (QLC01-02 and FP01-02) are in the range of 5.45–6.46 km/s under a depth of 20–68 km (0.9 GPa = 30 km), respectively. Observation of a dense linear broadband seismic array shows that V_S of the lower crust vary from 3.6 km/s to 3.75 km/s at the west QOB (Li et al., 2022). Here, our measured V_S of 6 schist (ZZ01-02, ZK01-02 and FYK01-02) are in the range of 3.11–4.01 km/s and those of 4 gneiss (QLC01-02 and FP01-02) are in the range of 2.98–4.00 km/s under a depth of 20–68 km (0.6–2.0 GPa), respectively. Our measured results are consistent with previous measured and observed results.

To further explore the effect of schist and gneiss on the composition and structure of the QOB, shear wave velocity structures below the two sampled points of the Zuikou and the Qilichuan (ZK and QLC) to a depth of 40 km (Zhao et al., 2021a,b) and below the three sampled points of Fengyukou, Zhouzhi, and Foping (FYK, ZZ, and FP) (Zhao et al., 2021a,b) from seismic ambient noise tomography were built and shown in Fig. 9. The changes in V_S with depth were calculated on the basis of the pressure coefficient and temperature coefficient of V_S (Table 2) to compare measured V_S with observed velocity profiles by seismology. The variation of the V_S of the ten rock samples with depth is presented in Fig. 8. The V_S of the rock samples are close to the velocity structures in the crust. The V_S of the samples from the Zhouzhi (ZZ) and Zuikou (ZK) changed from higher than the velocity structure to lower than the velocity structure at the middle – lower crust. The V_S of the samples from the Fengyukou (FYK), Qilichuan (QLC) and Foping (FP) are always lower than the velocity structures at the crust. The V_S of all samples are lower than the velocity structures at the upper mantle.

Obviously, the V_P and V_S of schist and gneiss measured in this work match the velocity of the middle and lower crust of the QOB, indicating that schist and gneiss are one of the important components of the QOB.

3.5. Origin of the low velocity zone of the QOB

For origin of the low velocity zone in the crust and mantle, main conclusions are including partially molten layers, an orientation of foliated-rocks/minerals, mantle-derived melts, and crustal shear zones. However, among those insights, melt and deformation/preferred orientation foliation rocks/minerals during tectonic shear movement are the two important factors.

Melts, characterized by zero shear modulus, have been usually used to explain origin of the low velocity zone in the crust and mantle (Selway and O'Donnell, 2019; Zhang et al., 2022). Seismic velocities of rocks by laboratory measurements (Popp and Kern, 1993; Ito and Tatsumi, 1995; Aizawa et al., 2002) and theoretical studies (Takei, 1998) suggested that the presence of fluid and/or melt cause significant decrease in velocity and hence results in the low velocity anomaly in the mid-to-lower crust (Zhao and Mizuno, 1999; Nakajima et al., 2001; Zhao et al., 2002). Experiment showed that about 0.2% melt could cause a low velocity zone with a shear wave velocity reduction of 5%–8% (Chantel et al., 2016). Crustal low velocity zone is observed broadly distributed beneath the interior of Tibetan Plateau and the presence of partial melting is proposed to account for its origin (Nelson et al., 1996; Owens and Zandt, 1997; Unsworth et al., 2005; Jiang et al., 2006; Le Pape et al., 2012; Yang et al., 2012; Xie et al., 2013).

Besides the melts, deformed foliated-rocks/minerals are though as another important origin for the low velocity zone. Analysis of teleseismic receiver functions show that seismic anisotropy of mylonites caused by the ductile flow in thrust shear zones are the reason of the low velocity layers in the Earth's crust beneath Eastern Siberia (Russia) and Central Mongolia (Zorin et al., 2002). The 3-D high-resolution crustal V_S and azimuthal anisotropy model by ambient noise tomography in the Pearl River Delta area of China reveal that the fast axes of the azimuthal anisotropy and low velocity zone mainly controlled by the regional shear stress field (Lü et al., 2023). The joint inversion of surface wave dispersion and receiver function data shown that discontinuous low velocity zone

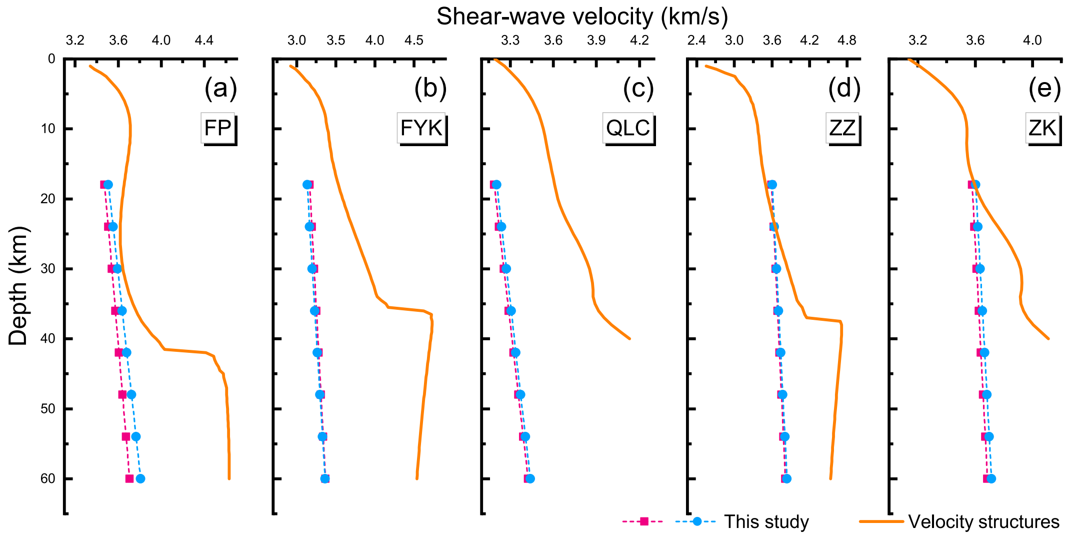

Fig. 9. The changes in wave velocities of rocks and velocity structures with depth. The wave velocities of rocks and velocity structures at the 5 sites of Foping (FP) (a), Fengyukou (FYK) (b), Qilichuan (QLC) (c), Zhouzhi (ZZ) (d), and Zuikou (ZK) (e) (Magenta and blue lines represent samples of numbers 01 and 02 from the same region, respectively). Orange lines were velocity structures from seismological observation (ZK and QLC referenced from Zhao et al. (2021a,b), and FYK, ZZ, and FP from Zhao et al. (2021a,b)). (For interpretation of the references to colour in this figure legend, the reader is referred to the web version of this article.)

Table 2
The pressure and temperature coefficients of V_S and V_P.

Sample	V_{S0} (km/s)	Pressure coefficient (km/(s·GPa))	Temperature coefficient (-10^{-4} km/(s·°C))	V_{P0} (km/s)	Pressure coefficient (km/(s·GPa))	Temperature coefficient (-10^{-4} km/(s·°C))
	V_S			V_P		
FP01	3.37	0.1791	3.688	5.85	0.1872	0.773
FP02	3.38	0.2318	4.857	5.91	0.2342	1.190
FYK01	3.08	0.1556	2.557	5.61	0.1981	0.718
FYK02	3.04	0.1764	3.570	5.66	0.2478	0.777
QLC01	3.09	0.1831	1.415	5.59	0.2464	1.055
QLC02	3.11	0.1806	1.487	5.63	0.2496	1.396
ZZ01	3.50	0.1680	3.809	6.06	0.1923	0.854
ZZ02	3.50	0.1826	4.082	6.00	0.2013	0.912
ZK01	3.53	0.0818	2.036	5.90	0.1231	1.157
ZK02	3.56	0.0852	2.036	5.93	0.1231	1.018

with up to 10% velocity reduction is present in the most parts of the mid-crust under the Tibetan Plateau and indicated that the low velocity zone is a result of mechanical deformation instead of magmatic activities (Tseng et al., 2009; Xu et al., 2013). The low velocity of the upper layer in the subducting oceanic crust in the North Qilian suture zone, NW China can be explained by the existence of deformed blueschist and foliated eclogite (Cao et al., 2013).

Low velocity zones are widely distributed over the QOB (Zhao et al., 2021a,b). The high and low velocity zones are interphase distributed and inclined to the eastern direction in the mantle of the Qinling orogenic belt (Matte et al.,1985; Song et al., 2018). Local seismic wave velocity anomalies in the lower crust can be clearly observed in the western QOB by multifrequency receiver function and surface wave data (Wei et al., 2020), however, the low velocity zones are not continuous (Guo and Chen, 2016). The high-resolution 3-D crust structure of QOB showed a low velocity area with an approximately N–S trend in the lower-middle crust (20–40 km) (Song et al., 2017). The ambient noise data show low velocities in the lower crust and uppermost mantle beneath the eastern QOB (Zhao et al., 2021a,b). The presence of significant low velocity anomalies in the uppermost mantle under the QOB was detected by teleseismic P-wave tomography (Lei and Zhao, 2016; Dong and Teng, 2018). The joint inversion of the surface wave dispersion and reception function of dense linear broadband seismic arrays indicates significant wave velocity anomalies extending to about 250 km depth below the QOB (Li et al., 2022). The two low-velocity bodies at a depth of 20 km of the central QOB were observed with a maximum perturbation of about −2% (Li et al., 2023).

And, for origin of the low velocity zone in the QOB, key insights include melt of hydrous minerals or rock (Zhao et al., 1996), deep crustal/mantle flow (Wang et al., 2018; Li et al., 2022, 2023), lithospheric deformation caused by tectonic stresses that could be linked to eastward extrusion of the Tibet Plateau (Molnar and Tapponnier, 1975) and the delamination of the lower crust (Li et al., 2023), the upwelling of hot materials in the big mantle wedge formed by the deep subduction of the Indian slab down to the mantle transition zone (Lei and Zhao, 2016; Lei et al., 2019).

However, as for the QOB, the magmatism quiescence during the Cenozoic (Ratschbacher et al., 2003), relatively low surface heat flow compared with volcanic areas (Hu et al., 2000) and mean no heating from the asthenosphere. Furthermore, the crustal thickness beneath the Qinling belt is ~40 km, which makes the increased heat production −melts-may not be the origin of low velocity zone of the QOB (Guo and Chen, 2016). Another possible explanation for the low velocity is the intruded lower crustal materials from the Tibetan Plateau (Clark and Royden, 2000; Enkelmann et al., 2006). However, this model is not supported by the low crustal V_P/V_S ratio (Hacker et al., 2000; Pan and Niu, 2011; Wang et al.,

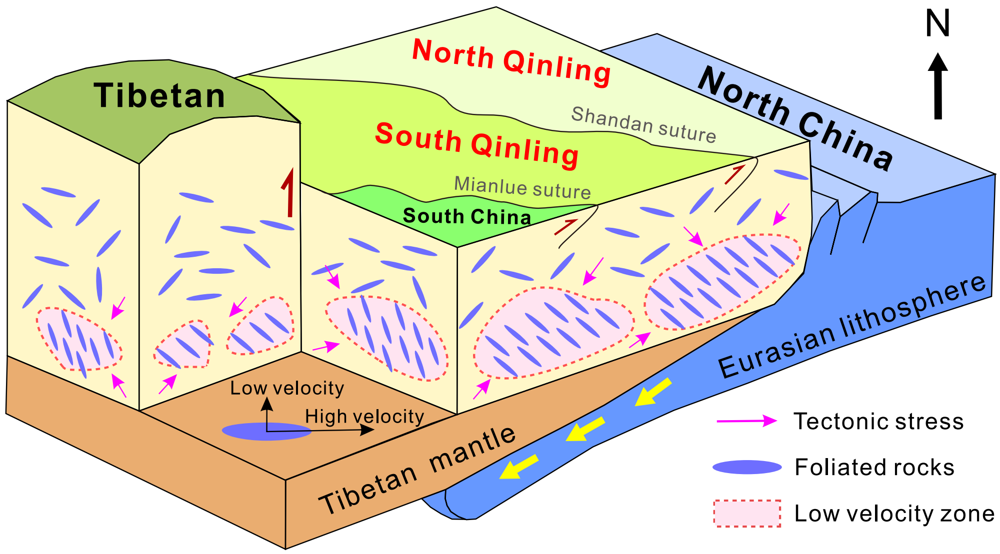

Fig. 10. Schematic mode of the origin of the low velocity zone in the QOB.

2014; Fig. 6). Therefore, the origin of the low velocity zone of the QOB are still not well defined. However, we proposed a new different insight for origin of the low velocity zone of the QOB here.

The QOB has experienced significant tectonic activity since the Cretaceous period, including ductile flow, strike-slip faults, and widespread extension and shear movement (Matte et al., 1985; Zhang et al., 1989; Liu et al., 1997; Ratschbacher et al., 2003; Enkelmann et al., 2006). Inverting arrival times from local earthquakes that occurred in the Qinling and surrounding region shown that crustal channel flow cannot exist in the whole Qinling orogenic belt and proposed that the localized low-velocity zone related to the orogenic activities (Ozacar and Zandt, 2004; Yang et al., 2012, 2022; Xie et al., 2013). Furthermore, ambient noise tomographic images show no continuous low-velocity zone is observed in the lower crust beneath the western QOB (Xie et al., 2013; Tang et al., 2015). Therefore, we proposed that the origin of the low velocity zone of the QOB should be related to the regional shear movement.

The V_P and V_S of schist and gneiss measured in this work match the velocity of the middle and lower crust of the QOB and also indicate that schist and gneiss are one of the important components of the QOB. Velocity anisotropy is proposed as a main cause of the anomalous high velocities although the crossing profiles show that such velocities are observed in different directions (Lee et al., 2022). Our measured wave velocities of schist and gneiss show obvious seismic anisotropy with 1.64%–17.42% for V_S and 2.93%–14.78% for V_P under conditions of crust and upper mantle, and wave velocities of a rock samples show different values in different structural directions. Therefore, orientation-arranged schist and gneiss caused by tectonic stress might lead to interlayer distribution of the high and low wave velocity zones. As discussed above, V_S of the samples is lower than the velocity structure in the middle to lower crust and the upper mantle (Fig. 9). So we proposed a schematic mode (Fig. 10) here that orientation-arranged schist and gneiss during regional shear deformation may be one of the important origins of the low velocity zone in the QOB.

4. Conclusions

The V_P and V_S of the Ten rock samples (gneiss and schist) from the Qinling orogenic belt (QOB) were measured under 0.6–2.0 GPa and 100–550 °C. The wave velocities increase with increasing pressure and decreasing temperature. The V_P and V_S of the schist and gneiss measured in this study match the velocity of the middle and lower crust of the QOB, indicating that schist and gneiss are important component of the QOB. All the schist and gneiss samples analyzed in this work exhibit obvious seismic anisotropy with 1.64%–17.42% for V_S and 2.93%–14.78% for V_P under conditions of crust and upper mantle. The CPO/LPO and layering distribution of mica in rock samples are the main reasons for this anisotropy. The V_S structures below the five sampled sites from seismic ambient noise tomography were built to explore the effect of schist and gneiss on the composition and structure of the QOB. The results indicate that orientation-arranged gneiss and schist caused by the tectonic activity might be the important origin of the character of V_P/V_S, seismic anisotropy, and the low velocity zone in the QOB. And, besides the melts, orientation-arranged layered rocks driven by the tectonic activities might be a new origin of the seismic anisotropy and the discontinuity of wave velocity in the Earth's interior.

CRediT authorship contribution statement

Lei Liu: Writing – original draft, Validation, Methodology, Investigation, Funding acquisition, Conceptualization. **Ying Li:** Writing – review & editing, Supervision, Resources, Conceptualization. **Tingting Li:** Investigation, Data curation. **Hanyu Wang:** Writing – original draft, Validation, Data curation. **Shasha Liu:** Software, Resources, Data curation. **Panpan Zhao:** Writing – review & editing, Validation, Resources. **Gerile Naren:** Resources, Data curation. **Li Yi:** Validation, Methodology, Conceptualization. **Hong Liu:** Validation, Methodology, Conceptualization. **Fengxia Sun:** . **Jianguo Du:** Writing – review & editing, Methodology, Conceptualization.

Data availability

The authors declare that the main data supporting the findings of this study are contained within the paper. All other relevant data are available from Mendeley Data https://data.mendeley.com/preview/g8wgt4yxb5?a=a1fd987d-415d-4df5-a05d-9794763ed81c.

Declaration of competing interest

The authors declare that they have no known competing financial interests or personal relationships that could have appeared to influence the work reported in this paper.

Acknowledgments

This research is supported by the National Natural Science Foundation of China (42174115 and 42330311), the Special Fund of the Institute of Earthquake Forecasting, China Earthquake Administration (CEAIEF20230301), and the State key laboratory of earthquake dynamics (LED2021B02). This research is a contribution to the International Geoscience Programme (IGCP) Project 724.

References

Aizawa, Y., Ito, K., Tatsumi, Y., 2002. Compressional wave velocity of granite and amphibolite up to melting temperatures at 1 GPa. Tectonophysics 351, 255–261. https://doi.org/10.1016/S0040-1951(02)00251-2.

Almqvist, B., Mainprice, D., 2017. Seismic properties and anisotropy of the continental crust: predictions based on mineral texture and rock microstructure. Rev. Geophys. 55 (2), 367–433. https://doi.org/10.1002/2016RG000552.

Bao, X., Song, X., Li, J., 2015. High-resolution lithospheric structure beneath Mainland China from ambient noise and earthquake surface-wave tomography. Earth Planet. Sci. Lett. 417, 132–141. https://doi.org/10.1016/j.epsl.2015.02.024.

Bazargan, M., Motra, H., Almqvist, B., Piazolo, S., Hieronymus, C., 2021. Pressure, temperature and lithological dependence of seismic and magnetic susceptibility anisotropy in amphibolites and gneisses from the central Scandinavian Caledonides. Tectonophysics 820, 229113. https://doi.org/10.1016/j.tecto.2021.229113.

Birch, F., 1961. The velocity of compressional waves in rocks to 10 kilobars: Part 2. J. Geophys. Res. 66 (7), 2199–2224. https://doi.org/10.1029/JZ066i007p02199.

Cao, Y., Jung, H., Song, S., 2013. Petro-fabrics and seismic properties of blueschist and eclogite in the North Qilian suture zone, NW China: Implications for the low-velocity upper layer in subducting slab, trench-parallel seismic anisotropy, and eclogite detectability in the subduction zone. J. Geophys. Res. Solid Earth 118, 3037–3058. https://doi.org/10.1002/jgrb.50212.

Chantel, J., Manthilake, G., Andrault, D., Novella, D., Yu, T., Wang, Y.B., 2016. Experimental evidence supports mantle partial melting in the asthenosphere. Sci. Adv. 2 (5), e1600246. https://doi.org/10.1126/sciadv.1600246.

Christensen, N.I., 1965. Compressional wave velocities in metamorphic rocks at pressures to 10 kilobars. J. Geophys. Res. 70, 6147–6164. https://doi.org/10.1029/JZ070i024p06147.

Christensen, N., Mooney, W., 1995. Seismic velocity structure and composition of the continental crust: a global view. J. Geophys. Res. 100, 9761–9788. https://doi.org/10.1029/95JB00259.

Clark, M.K., Royden, L.H., 2000. Topographic ooze: building the eastern margin of Tibet by lower crustal flow. Geology 28 (8), 703–706. https://doi.org/10.1130/0091-7613(2000)28<703:TOBTEM>2.0.CO;2.

Dong, X., Teng, J., 2018. Traveltime tomography using teleseismic P wave in the northeastern Tibetan plateau. Chinese J. Geophys. 61, 2066–2074. https://doi.org/10.6038/cjg2018K0214.

Enkelmann, E., Ratschbacher, L., Jonckheere, R., Nestler, R., Fleischer, M., Gloaguen, R., Hacker, B.R., Zhang, Y.Q., Ma, Y.-S., 2006. Cenozoic exhumation and deformation of northeastern Tibet and the Qinling: is Tibetan lower crustal flow diverging around the Sichuan Basin? Geol. Soc. Am. Bull 118, 651–671. https://doi.org/10.1130/B25805.

Fouch, M.J., Rondenay, S., 2006. Seismic anisotropy beneath stable continental interiors. Phys. Earth and Planet. Inter. 158, 292–320. https://doi.org/10.1016/j.pepi.2006.03.024.

Gao, Y., Chen, L., Wang, X., Ai, Y., 2019. Complex lithospheric deformation in eastern and northeastern Tibet from shear wave splitting observations and its geodynamic implications. J. Geophys. Res. Solid Earth 124, 10331–10346. https://doi.org/10.1029/2018JB017081.

Guo, Z., Chen, Y.J., 2016. Crustal structure of the eastern Qinling orogenic belt and implication for reactivation since the Cretaceous. Tectonophysics 683, 1–11. https://doi.org/10.1016/j.tecto.2016.06.007.

Hacker, B.R., Gnos, E., Ratschbacher, L., Grove, M., Mcwilliams, M., Sobolev, S.V., Wan, J., Zhenhan, W., 2000. Hot and dry deep crustal xenoliths from Tibet. Science 287, 2463–2466. https://doi.org/10.1126/science.287.5462.2463.

Han, C., Hammond, J.O.S., Ballmer, M.D., Wei, W., Xu, M., Huang, Z., Wang, L., 2024. Multi-scale anisotropy in NE China: evidence for localized mantle upwelling. Earth Planet. Sci. Lett. 625, 118495. https://doi.org/10.1016/j.epsl.2023.118495.

Hu, S., He, L., Wang, J., 2000. Heat flow in the continental area of China: a new data set. Earth Planet. Sci. Lett. 179, 407–419. https://doi.org/10.1016/S0012-821X(00)00126-6.

Huang, Z., Xu, M., Wang, L., Mi, N., Yu, D., Li, H., 2008. Shear wave splitting in the southern margin of the Ordos Block, north China. Geophys. Res. Lett. 35, 2008GL035188. https://doi.org/10.1029/2008GL035188.

Hyndman, R.D., Drury, M.J., 1976. The physical properties of oceanic basement rocks from deep drilling on the Mid-Atlantic Ridge. J. Geophys. Res. 81, 4042–4052. https://doi.org/10.1029/JB081i023p04042.

Ishikawa, M., Arima, M., 2009. Laboratory measurements of ultrasonic wave velocities of crustal rocks at high pressures and temperatures: Petrological structure of Izu-Bonin-Mariana arc crust. In: Gupta, A.K., Dasgupta, S. (Eds.), Physics and Chemistry of the Earth's Interior. Springer, New York, pp. 143–152. https://doi.org/10.1007/978-1-4419-0346-4_8.

Ito, K., Tatsumi, Y., 1995. Measurement of elastic wave velocities in granulite and amphibolite having identical H_2O-free bulk compositions up to 850 C at 1 GPa. Earth Planet. Sci. Lett. 133, 255–264. https://doi.org/10.1016/0012-821X(95)00074-M.

Ji, S., Salisbury, M., 1993. Shear-wave velocities, anisotropy and splitting in high-grade mylonites. Tectonophysics 221, 453–473. https://doi.org/10.1016/0040-1951(93)90173-H.

Jiang, M., Galvé, A., Hirn, A., de Voogd, B., Laigle, M., Su, H.P., Diaz, J., Lépine, J.C., Wang, Y.X., 2006. Crustal thickening and variations in architecture from the Qaidam basin to the Qiang Tang (North-Central Tibetan Plateau) from wide-angle reflection seismology. Tectonophysics 412, 121–140. https://doi.org/10.1016/j.tecto.2005.09.011.

Kern, H., Ivankina, T.I., Nikitin, A.N., Lokajíček, T., Pros, Z., 2008. The effect of oriented microcracks and crystallographic and shape preferred orientation on bulk elastic anisotropy of a foliated biotite gneiss from Outokumpu. Tectonophysics 457, 143–149. https://doi.org/10.1016/j.tecto.2008.06.015.

Kern, H., Popp, T., Gorbatsevich, F., Zharikov, A., Lobanov, K., Smirnov, Y., 2001. Pressure and temperature dependence of V_P and V_S in rocks from the superdeep well and from surface analogues at Kola and the nature of velocity anisotropy. Tectonophysics 338, 113–134. https://doi.org/10.1016/S0040-1951(01)00128-7.

Khazanehdari, J., Rutter, E.H., Brodie, K.H., 2000. High-pressure-high-temperature seismic velocity structure of the midcrustal and lower crustal rocks of the Ivrea-Verbano zone and Serie dei Laghi, NW Italy. J. Geophys. Res.-Solid Earth 105 (B6), 13843–13858. https://doi.org/10.1029/2000JB900025.

Kitamura, K., 2006. Constraint of lattice-preferred orientation (LPO) on V_P anisotropy of amphibole-rich rocks. Geophys. J. Int. 165, 1058–1065. https://doi.org/10.1111/j.1365-246X.2006.02961.x.

Le Pape, F., Jones, A.G., Vozar, J., Wei, W.B., 2012. Penetration of crustal melt beyond the Kunlun Fault into northern Tibet. Nat. Geosci. 5, 330–335. https://doi.org/10.1038/NGEO1449.

Lee, H., Bezada, M.J., Kim, Y., 2022. The origin of the low-velocity anomalies beneath the rootless Atlas Mountains: insights gained from modeling of anisotropy developed by the travel of Canary Plume. J. Geophys. Res. Solid Earth 127, e2022JB024622. https://doi.org/10.1029/2022JB024622.

Lee, H.-Y., Gung, Y., Chen, L.-W., Chen, W.-S., Chen, Y.-N., Cai, S.-J., Chen, H.-C., Liao, C.-W., 2023. Strong variation of near-surface seismic anisotropy in Taiwan and its geological implications. Earth Planet. Sci. Lett. 620, 118339. https://doi.org/10.1016/j.epsl.2023.118339.

Lei, J., Zhao, D., 2016. Teleseismic P-wave tomography and mantle dynamics beneath Eastern Tibet. Geochem. Geophys. Geosyst. 17, 1861–1884. https://doi.org/10.1002/2016GC006262.

Lei, J., Zhao, D., Xu, X., Xu, Y., Du, M., 2019. Is there a big mantle wedge under eastern Tibet? Phys. Earth Planet. Inter. 292, 100–113. https://doi.org/10.1016/j.pepi.2019.04.005.

Li, Y.K., Gao, R., Gao, J.W., Mi, S.X., Yao, Y.T., Li, W.H., Xiong, X.S., 2015. Characteristics of crustal velocity structure along Qinling orogenic belt. Prog. Geophys. 30, 1056–1069. https://doi.org/10.10638/pg20150309.

Li, M., Liu, S., Yang, D., Xie, C., Xu, X., Dong, G., Wang, W., Yang, S., 2023. Deformation of the Qinling belt revealed by P -wave velocity and azimuthal anisotropy tomography. Geophys. J. Int. 234 (1), 263–279. https://doi.org/10.1093/gji/ggad069.

Li, H., Ye, Z., Gao, R., Huang, X., 2022. A distinct contrast in the lithospheric structure and limited crustal flow across the northeastern Tibetan Plateau: Evidence from Vs and Vp/Vs imaging. Tectonophysics 836, 229413. https://doi.org/10.1016/j.tecto.2022.229413.

Lin, F.C., Ritzwoller, M.H., Yang, Y.J., Moschetti, M.P., Fouch, M.J., 2011. Complex and variable crustal and uppermost mantle seismic anisotropy in the western United States. Nat. Geosci. 4, 55–61. https://doi.org/10.1038/NGEO1036.

Liu, Y.S., Gao, S., Jin, S.Y., Hu, S.H., Sun, M., Zhao, Z.B., Feng, J.L., 2001. Geochemistry of lower crustal xenoliths from Neogene Hannuoba basalt, North China craton: implications for petrogenesis and lower crustal composition. Geochim. Cosmochim. Acta 65, 2589–2604. https://doi.org/10.1016/S0016-7037(01)00609-3.

Liu, J.H., Liu, F.T., Sun, R.M., Wu, H., Wu, D., 1997. Seismic tomography beneath the Qinling Dabie orogenic belts and both the northern and southern fringes. Acta Geophys. Sin. 38, 46–54 (in Chinese).

Liu, M., Mooney, W.D., Li, S., Okaya, N., Detweiler, S., 2006. Crustal structure of the northeastern margin of the Tibetan plateau from the Songpan-Ganzi terrane to the Ordosbasin. Tectonophysics 420, 253–266. https://doi.org/10.1016/j.tecto.2006.01.025.

Liu, Y., Xie, H., Guo, J., Zhou, W., Xu, J., Zhao, Z., 2000. A new method for experimental determination of compressional velocities in rocks and minerals at high-pressure. Chinese Phys. Lett. 17, 924–926. https://doi.org/10.1088/0256-307X/17/12/024.

Liu, Y., Xie, H., Zhou, W., Guo, J., 2002. A method for experimental determination of compressional velocities in rocks and minerals at high pressure and high temperature. J. Phys.: Condens Matter 14, 11381–11384. https://doi.org/10.1088/0953-8984/14/44/486.
Long, M.D., 2013. Constraints on subduction geodynamics from seismic anisotropy. Rev. Geophys. 51, 76–112. https://doi.org/10.1002/rog.20008.
Long, M.D., Becker, T.W., 2010. Mantle dynamics and seismic anisotropy. Earth Planet. Sci. Lett. 297, 341–354. https://doi.org/10.1016/j.epsl.2010.06.036.
Lü, Z., Ye, X., Zhang, Y., Qian, Y., Wen, G., 2023. 3-D crustal shear wave velocity and azimuthally anisotropic structure of the Pearl River Delta onshore-offshore area and its tectonic implications. Tectonophysics 868, 230097. https://doi.org/10.1016/j.tecto.2023.230097.
Matte, P., Malavieille, J., Tapponnier, P., Maluski, H., Qin, X., Lun, L., Qin, T., 1985. Tectonics of the Qinling Belt: build-up and evolution of eastern Asia. Nature 317, 496–500. https://doi.org/10.1038/317496a0.
Meng, Q.R., Zhang, G.W., 2000. Geologic framework and tectonic evolution of the Qinling orogen, central China. Tectonophysics 323, 183–196. https://doi.org/10.1016/S0040-1951(00)00106-2.
Miller, D.J., Christensen, N.I., 1997. Seismic velocities of lower crustal and upper mantle rocks from the slow-spreading Mid-Atlantic Ridge, south of the Kane Transform Zone (MARK). Proc. Ocean Drill. Program Sci. Results 153, 437–454. https://doi.org/10.2973/odp.proc.sr.153.043.1997.
Molnar, P., Tapponnier, P., 1975. Cenozoic tectonics of Asia: effects of a continental collision: features of recent continental tectonics in Asia can be interpreted as results of the India-Eurasia collision. Science 189, 419–426. https://doi.org/10.1126/science.189.4201.419.
Nábělek, J., Hetényi, G., Vergne, J., Sapkota, S., Kafle, B., Jiang, M., Su, H., Chen, J., Huang, B.S., the Hi-Climb Team, 2009. Underplating in the Himalaya-Tibet Collision Zone revealed by the Hi-CLIMB experiment. Science 325, 1371–1374. https://doi.org/10.1126/science.1167719.
Nakajima, J., Matsuzawa, T., Hasegawa, A., Zhao, D.P., 2001. Seismic imaging of arc magma and fluids under the central part of northeastern Japan. Tectonophysics 341, 1–17. https://doi.org/10.1016/S0040-1951(01)00181-0.
Nelson, K.D., Zhao, W.J., Brown, L.D., Kuo, J., Che, J.K., Liu, X.W., Klemperer, S.L., Makovsky, Y., Meissner, R., Mechie, J., Kind, R., Wenzel, F., Ni, J., Nabelek, J., Chen, L.S., Tan, H.D., Wei, W.B., Jones, A.G., Booker, J., Unsworth, M., Kidd, W.S.F., Hauck, M., Alsdorf, D., Ross, A., Cogan, M., Wu, C.D., Sandvol, E., Edwards, M., 1996. Partially molten middle crust beneath southern Tibet: synthesis of project INDEPTH results. Science 274, 1684–1688. https://doi.org/10.1126/science.274.5293.1684.
Owens, T., Zandt, G., 1997. Implications of crustal property variations for model of Tibetan Plateau evolution. Nature 387, 37–43. https://doi.org/10.1038/387037a0.
Ozacar, A.A., Zandt, G., 2004. Crustal seismic anisotropy in central Tibet: implications for deformational style and flow in the crust. Geophys. Res. Lett. 31, L23601. https://doi.org/10.1029/2004GL021096.
Pan, S., Niu, F., 2011. Large contrasts in crustal structure and composition between the Ordos plateau and the NE Tibetan plateau from receiver function analysis. Earth Planet. Sci. Lett. 303, 291–298. https://doi.org/10.1016/j.epsl.2011.01.007.
Popp, T., Kern, H., 1993. Thermal dehydration reactions characterized by combined measurements of electrical conductivity and elastic wave velocities. Earth Planet. Sci. Lett. 120, 43–57. https://doi.org/10.1016/0012-821X(93)90022-2.
Priestley, K., Ho, T., Takei, Y., McKenzie, D., 2024. The thermal and anisotropic structure of the top 300 km of the mantle. Earth Planet. Sci. Lett. 626, 118525. https://doi.org/10.1016/j.epsl.2023.118525.
Ratschbacher, L., Hacker, B.R., Calvert, A., Webb, L.E., Grimmer, J.C., McWilliams, M. O., Ireland, T., Dong, S., Hu, J., 2003. Tectonics of the Qinling (Central China): tectonostratigraphy, geochronology, and deformation history. Tectonophysics 366, 1–53. https://doi.org/10.1016/S0040-1951(03)00053-2.
Schulte-Pelkum, V., Monsalve, G., Sheehan, A., Pandey, M.R., Sapkota, S., Bilham, R., Wu, F., 2005. Imaging the Indian subcontinent beneath the Himalaya. Nature 435, 1222–1225. https://doi.org/10.1038/nature03678.
Selway, K., O'Donnell, J.P., 2019. A small, unextractable melt fraction as the cause for the low velocity zone. Earth Planet. Sci. Lett. 517, 117–124. https://doi.org/10.1016/j.epsl.2019.04.012.
Silver, P.G., 1996. Seismic anisotropy beneath the continents: probing the depths of geology. Annu. Rev. Earth Planet. Sci. 24, 385–432. https://doi.org/10.1146/annurev.earth.24.1.385.
Song, P., Zhang, X., Liu, Y., Teng, J., 2017. Moho imaging based on receiver function analysis with teleseismic wavefield reconstruction: Application to South China. Tectonophysics 718, 118–131. https://doi.org/10.1016/j.tecto.2017.05.031.
Song, P., Teng, J., Zhang, X., Liu, Y., Si, X., Ma, X., Qiao, Y., Dong, X., 2018. Flyover crustal structures beneath the Qinling Orogenic Belt and its tectonic implications. J. Geophys. Res. Solid Earth 123, 6703–6718. https://doi.org/10.1029/2017JB015401.
Takei, Y., 1998. Constitutive mechanical relations of solid-liquid composites in terms of grain-boundary contiguity. J. Geophys. Res.-Solid Earth 103, 18183–18203. https://doi.org/10.1029/98JB01489.
Tang, Y., Zhou, S., Chen, Y.J., Sandvol, E., Liang, X., Feng, Y., Jin, G., Jiang, M., Liu, M., 2015. Crustal structures across the western Weihe Graben, North China: implications for extrusion tectonics at the northeast margin of Tibetan Plateau. J. Geophys. Res. Solid Earth 120 (7), 5070–5081. https://doi.org/10.1002/2014JB011210.
Tarkov, A.P., Vavakin, V.V., 1982. Poisson's ratio behaviour in various crystalline rocks: application to the study of the Earth's interior. Phys. Earth Planet. Inter. 29, 24–29. https://doi.org/10.1016/0031-9201(82)90134-0.
Teng, J.W., Li, S.L., Zhang, Y., Wang, F.Y., Pi, J.L., Junmeng, Z., Zhang, C.K., Qiao, Y.H., Hu, G.Z., Yan, Y.-F., 2014. Fine velocity structures and deep processes in crust and mantle of the Qinling orogenic belt and the adjacent North China craton and Yangtze craton. Chinese J. Geophys. 57, 3154–3175. https://doi.org/10.6038/cjg20141006.
Tseng, T.L., Chen, W.P., Nowack, R.L., 2009. Northward thinning of Tibetan crust revealed by virtual seismic profiles. Geophys. Res. Lett. 36, L24304. https://doi.org/10.1029/2009GL040457.
Unsworth, M.J., Jones, A.G., Wei, W., Marquis, G., Gokarn, S.G., Spratt, J.E., Team, I.-M., 2005. Crustal rheology of the Himalaya and Southern Tibet inferred from magnetotelluric data. Nature 438, 78–81. https://doi.org/10.1038/nature04154.
Wang, Z., Fu, G., She, Y., 2018. Crustal density structure, lithosphere flexure mechanism, and isostatic state throughout the Qinling Orogen revealed by in situ dense gravity observations. J. Geophys. Res. Solid Earth 123 (11), 10026–10039. https://doi.org/10.1029/2018JB016117.
Wang, Q., Ji, S., Salisbury, M.H., Xia, B., Pan, M., Xu, Z., 2005a. Pressure dependence and anisotropy of P-wave velocities in ultrahigh-pressure metamorphic rocks from the Dabie-Sulu orogenic belt (China): Implications for seismic properties of subducted slabs and origin of mantle reflections. Tectonophysics 398, 67–99. https://doi.org/10.1016/j.tecto.2004.12.001.
Wang, T., Pei, X., Wang, X., Hu, N., Li, W., Zhang, G., 2005b. Orogen-parallel westward oblique uplift of the Qinling basement complex in the core of the Qinling Orogen (China): an example of oblique extrusion of deep-seated metamorphic rocks in a collisional orogen. J. Geol. 113, 181–200. https://doi.org/10.1086/427668.
Wang, C.Y., Sandvol, E., Zhu, L., Lou, H., Yao, Z., Luo, X., 2014. Lateral variation of crustal structure in the Ordos block and surrounding regions, North China, and its tectonic implications. Earth Planet. Sci. Lett. 387, 198–211. https://doi.org/10.1016/j.epsl.2013.11.033.
Wang, T., Wang, X., Tian, W., Zhang, C., Li, W., Li, S., 2009. North Qinling Paleozoic granite associations and their variation in space and time: implications for orogenic processes in the orogens of central China. Sci. China Ser. D-Earth Sci. 52, 1359–1384. https://doi.org/10.1007/s11430-009-0129-5.
Wei, Z., Li, Z., Chen, L., Chu, R., Wu, S., Ling, Y., Zeng, Q., 2020. Crustal structure underneath central China across the Tibetan Plateau, the North China Craton, the South China Block and the Qinling-Dabie Orogen constrained by multifrequency receiver function and surface wave data. J. Asian Earth Sci. 202, 104535. https://doi.org/10.1016/j.jseaes.2020.104535.
Wei, W., Zhao, D., Xu, J., Zhou, B., Shi, Y., 2016. Depth variations of P-wave azimuthal anisotropy beneath Mainland China. Sci. Rep. 6, 29614. https://doi.org/10.1038/srep29614.
Xie, J.Y., Ritzwoller, M.H., Shen, W.S., Yang, Y.J., Zheng, Y., Zhou, L.Q., 2013. Crustal radial anisotropy across Eastern Tibet and the Western Yangtze Craton. J. Geophys. Res.-Solid Earth 118, 4226–4252. https://doi.org/10.1002/jgrb.50296.
Xie, H.S., Zhang, Y.M., Xu, H.G., Hou, W., Guo, J., Zhao, H.R., 1993. A new method of measurement for elastic wave velocities in minerals and rocks at high temperature and high pressure and its significance. Sci. China Chem. 36, 1276–1280.
Xu, Z., Song, X., Zhu, L., 2013. Crustal and uppermost mantle S velocity structure under Hi-CLIMB seismic array in central Tibetan Plateau from joint inversion of surface wave dispersion and receiver function data. Tectonophysics 584, 209–220. https://doi.org/10.1016/j.tecto.2012.08.024.
Xue, F., Kröner, A., Reischmann, T., Lerch, F., 1996. Palaeozoic pre- and post-collision calc-alkaline magmatism in the Qinling orogenic belt, central China, as documented by zircon ages on granitoid rocks. J. Geol. Soc. London 153, 409–417. https://doi.org/10.1144/gsjgs.153.3.0409.
Yang, T., Monna, S., Fang, L., 2022. Seismic imaging of the crust and uppermost mantle structure in the Qinling orogenic belt and its surroundings: Geodynamic implications. Tectonophysics 843, 229619. https://doi.org/10.1016/j.tecto.2022.229619.
Yang, Y.J., Ritzwoller, M.H., Zheng, Y., Shen, W.S., Levshin, A.L., Xie, Z.J., 2012. A synoptic view of the distribution and connectivity of the mid-crustal low velocity zone beneath Tibet. J. Geophys. Res.-Solid Earth, 117. https://doi.org/10.1029/2011JB008810.
Ye, Z., Li, J., Gao, R., Song, X., Li, Q., Li, Y., Xu, X., Huang, X., Xiong, X., Li, W., 2017. Crustal and uppermost mantle structure across the Tibet-Qinling transition zone in NE Tibet: implications for material extrusion beneath the Tibetan plateau. Geophys. Res. Lett. 44 (20), 10316–10323. https://doi.org/10.1002/2017GL075141.
You, Z., Han, Y., Suo, S., Chen, N., Zhong, Z., 1993. Metamorphic history and tectonic evolution of the Qinling Complex, eastern Qinling Mountains, China. J. Metamorph. Geol. 11, 549–560. https://doi.org/10.1111/j.1525-1314.1993.tb00171.x.
Yuan, X.C., 1996. Velocity structure of the Qinling lithosphere and mushroom cloud model. Sci. China Earth Sci. 39, 235–244 (in Chinese).
Zandt, G., Ammon, C., 1995. Continental crust composition constrained by measurements of crustal Poisson's Ratio. Nature 374, 152–154. https://doi.org/10.1038/374152a0.
Zertani, S., Vrijmoed, J.C., Tilmann, F., John, T., Andersen, T.B., Labrousse, L., 2020. *P* wave anisotropy caused by partial eclogitization of descending crust demonstrated by modeling effective petrophysical properties. Geochem. Geophys. Geosyst. 21, e2019GC008906. https://doi.org/10.1029/2019GC008906.
Zhang, G.W., Dong, Y., Yao, A.P., 1997. The crustal compositions, structures and tectonic evolution of the Qinling orogenic belt. Geol. Shaanxi 15, 1–14 (in Chinese with English abstract).

Zhang, B.H., Fei, H.Z., Ge, J.H., Zeng, L.S., Xia, Q.K., 2022. Crustal melting in orogenic belts revealed by eclogite thermal properties. Nat. Commun. 13, 4673. https://doi.org/10.1038/s41467-022-32484-w.

Zhang, S.Q., Karato, S., 1995. Lattice preferred orientation of olivine aggregates deformed in simple shear. Nature 375, 774–777. https://doi.org/10.1038/375774a0.

Zhang, F., Wu, Q., Li, Y., Zhang, R., Sun, L., Pan, J., Ding, Z., 2018. Seismic tomography of Eastern Tibet: implications for the Tibetan Plateau growth. Tectonics 37, 2833–2847. https://doi.org/10.1029/2018TC004977.

Zhang, G., Yu, Z., Sun, Y., Cheng, S., Li, T., Xue, F., Zhang, C., 1989. The major suture zone of the Qinling orogenic belt. J. Asian Earth Sci. 3, 63–76. https://doi.org/10.1016/0743-9547(89)90010-X.

Zhang, G., Zhang, B.R., Yuan, X.R., Xiao, Q.H., 2001. Qinling Orogenic Belt and Continental Dynamics. Science Publishing House, Beijing.

Zhao, P., Chen, J., Li, Y., Liu, Q., Chen, Y., Guo, B., Yin, X., 2021b. Growth of the Northeastern Tibetan Plateau driven by crustal channel flow: evidence from high-resolution ambient noise imaging. Geophys. Res. Lett. 48, e2021GL093387. https://doi.org/10.1029/2021GL093387.

Zhao, Z.D., Gao, S., Luo, T.C., Zhang, B.R., Xie, H.S., Zhang, Y.M., Xu, H.G., Guo, J., 1996. Origin of the crustal low velocity layer of Qinling and North China: Evidence from laboratory measurement of P-wave velocity in rocks at high PT conditions. Acta Geophys. Sin. 39, 650–652 https://qikan.cqvip.com/Qikan/Article/Detail?id=2247655.

Zhao, K., Luo, Y., Yang, Y., Yang, X., 2021a. High-resolution lithospheric structures of the Qinling-Dabie orogenic belt: implications for deep subduction and delamination of continental lithosphere. Tectonophysics 806, 228799. https://doi.org/10.1016/j.tecto.2021.228799.

Zhao, D.P., Mishra, O.P., Sanda, R., 2002. Influence of fluids and magma on earthquakes: seismological evidence. Phys. Earth Planet. Inter. 132, 249–267. https://doi.org/10.1016/S0031-9201(02)00082-1.

Zhao, D.P., Mizuno, T., 1999. Crack density and saturation rate in the 1995 Kobe earthquake region. Geophys. Res. Lett. 26, 3213–3216. https://doi.org/10.1029/1999GL005411.

Zhao, D., Yu, S., Liu, X., 2016. Seismic anisotropy tomography: new insight into subduction dynamics. Gondw. Res. 33, 24–43. https://doi.org/10.1016/j.gr.2015.05.008.

Zhou, W., Fan, D., Liu, Y., Xie, H., 2011. Measurements of wave velocity and electrical conductivity of an amphibolite from southwestern margin of the Tarim Basin at pressures to 1.0 GPa and temperatures to 700 ℃: Comparison with field observations. Geophys. J. Int. 187, 1393–1404. https://doi.org/10.1111/j.1365-246X.2011.05220.x.

Zhou, Z., Lei, J., 2016. Pn anisotropic tomography and mantle dynamics beneath China. Phys. Earth Planet. Inter. 257, 193–204. https://doi.org/10.1016/j.pepi.2016.06.005.

Zorin, Y.A., Mordvinova, V.V., Turutanov, E.K., Belichenko, B.G., Artemyev, A.A., Kosarev, G.L., Gao, S.S., 2002. Low seismic velocity layers in the Earth's crust beneath Eastern Siberia (Russia) and Central Mongolia: receiver function data and their possible geological implication. Tectonophysics 359, 307–327. https://doi.org/10.1016/S0040-1951(02)00531-0.

Zhang, G.W., Dong, Y.P., Lai, S.C., Guo, A. Meng Q.R., Liu, S.F., Chen, S.Y., Yao, A., Zhang, Z.Q., Pei, X.Z., Li, S.Z., 2004. Mianlue tectonic zone and Mianlue suture zone on southern margin of Qinling-Dabie orogenic belt. Science in China (Series D), 49 , 300-316. doi:10.1360/02YD0526.